*energies*

Article

# The Influence of Winglet Pitching on the Performance of a Model Wind Turbine: Aerodynamic Loads, Rotating Speed, and Wake Statistics

**Emmanuvel Joseph Aju, Dhanush Bhamitipadi Suresh and Yaqing Jin ***

Department of Mechanical Engineering, The University of Texas at Dallas, Richardson, TX 75080, USA; Emmanuvel.Aju@UTDallas.edu (E.J.A.); Dhanush.BhamitipadiSuresh@UTDallas.edu (D.B.S.)
* Correspondence: yaqing.jin@utdallas.edu; Tel.: +1-972-883-4218

Received: 30 July 2020; Accepted: 29 September 2020 ; Published: 6 October 2020

**Abstract:** The objective of this study is to investigate the influence of winglet pitching as an aero-brake on the performance of a model wind turbine by wind tunnel experiments. Time-resolved particle image velocimetry, force sensor, and datalogger were used to characterize the coupling between wake statistics, aerodynamic loads, and rotation speed. Results highlighted that, for a winglet with 4% of the rotor diameter length, the increase of its pitching angle can significantly reduce the turbine rotation speed up to ~28% and thrust coefficient of ~20%. The winglet pitching induced minor influence on the velocity deficit in the very near wake regions, while its influence on accelerating the wake recovery become clear around three diameters downstream the turbine rotor. The turbulence kinetic energy exhibited a distinctive increase under large pitching angles in the near wake region at the turbine hub height due to the strong vertical flow fluctuations. Further investigation on the spectra of wake velocities revealed that the pitching of winglet can suppress the high-pass filtering effects of turbines on wake fluctuations; such large-scale turbulence facilitated the flow mixing and accelerated the wake transport.

**Keywords:** winglet pitching; rotating speed; wake statistics; wind tunnel experiment

## 1. Introduction

Wind energy is one of the most abundantly available and fastest growing renewable energy sources in the US, which has increased more than six times during the last decade [1]. While wind turbines across various scales have been widely integrated in power grids, many engineering and scientific challenges still exist where the power generation cost is higher compared to traditional energy resources [2].

One of the most distinctive challenges for wind energy is the unsteadiness of incoming wind flows and therefore fluctuating power output and aerodynamic loads for wind turbines. Extensive studies [3–8] have pointed out that the atmospheric boundary layer varies continuously with season, time of the day, temperature, and other geophysical parameters. With wind tunnel and field measurement, recent works [9–12] have systematically investigated the influence of incoming flow fluctuations on the blade rotating speed and wake transport over both single turbine and wind farms. Specifically, under very high incoming velocities, the turbine rotating speed may exceed the rated value accompanied with dramatic aerodynamic loads. In such scenario, pitch control of turbine blades has been one of the mostly explored approaches for protecting the turbines under extreme wind conditions and optimize the wind turbine performance. By altering the effective angle of attacks and therefore the aerodynamic loads on blades, the pitching control allows for keeping constant turbine rotating speed and therefore power output at high wind speeds [13]. Nagai et al. [14] designed and constructed a prototype 3kW wind turbine generator with a variable pitch of the turbine blades. They found that it is not easy to maintain a constant rotational speed with wind fluctuation due to small moment of inertia of the turbine. They reported that the aerodynamic loads on the turbine can be significantly reduced by feathering the blades, which allows the structure to survive even under typhoon-like conditions. Muljadi and Butterfield [15] studied blade pitching in a variable speed wind turbine. They found that the capability of quick blade pitching is the key to maintaining constant rotor speed. To improve the pitch performance due to delays caused by hydraulic pressure driven units, Gao and Gao [16] developed a novel approach by integrating the delay–perturbation estimation and tested on turbines from kW to MW scales. In the last few decades, more attention has focused on the 'smart' blade pitching, where multiple control devices are equipped on a blade to adjust the local aerodynamic forces. Compared to the pitching of entire blade, 'smart' blade pitching allows faster responses to the incoming flow conditions and better suppresses the unsteady wind loads [17–19].

During recent decades, adding winglets on the blade tip has proven to be an effective approach to improve the turbine efficiency. With a small extension of the blade tip, winglets can effectively restrict the spanwise velocity, reduce the induced drag in the tip region, diminish wing tip vortices, and therefore lead to more favorable aerodynamics. Extensive efforts have focused on the role of winglets in improving the blade designs and increasing the power output. According to Whitcomb [20], the addition of a small winglet can reduce the induced drag loss more than double that reduced by increasing the wingspan with the same length. Johansen and Sørensen [21] studied different designs of winglets with the height of winglet being approximately 1.5% of rotor radius using computational fluid dynamics. They illustrated that, compared to upstream-facing winglets, the downstream-facing counterparts performed better with an increase of 1.71% in power coefficient and 1.81% in thrust coefficient at 10 m/s wind speed. They also reported that the power and thrust coefficients are highly dependent on tip-speed ratio and, for some designs, the winglets may reduce the power output at low wind speeds. Imamura et al. [22] numerically analyzed the horizontal axis wind turbine with winglets and blade tip extension. They showed that, compared to blade tip extension, rotors with winglets were more effective at decreasing the wake turbulence and increasing the power output. Gauna and Johansen [23] performed a theoretical study using an actuator cap with cylinders at the tips representing winglets. They demonstrated that the Lanchester–Betz–Joukowsky limit still holds for a wind turbine with winglets, and the increase in power production is due to the reduction in tip losses. Experimental work by Saravanan et al. [24,25] explored the effect of winglet at the tip of the blade on a wind turbine. They found that the pressure difference on the wind turbine blade increased due to the presence of the winglet. They also stated that pressure difference increases with longer winglet or smaller curvature radius of the winglet. Belferhat et al. [26] studied the flow over an isolated wing equipped with a small winglet. Their study involved different winglet cant angles of 0°, 55°, 65°, and 75° and reported that winglet cant angle of 55° performed the best for increasing the power production. Wind tunnel experiments by Tobin et al. [27] found that, with a winglet of 6.7% rotor radius length, the power coefficient and thrust of the turbine can increase up to 8.2% and 15%. Zhu et al. [28] numerically investigated both upwind and downwind winglets on a horizontal axis wind turbine. They illustrated that, under tip-speed-ratio of 7 and blade pitch angle at 15°, the upwind winglet produced higher power than the downwind counterpart. With both numerical and experimental efforts, Khaled et al. [29] reported that at a cant angle of 48.3° and winglet length 6.32% of the rotor radius, the turbine showed the maximum power and thrust increase of 8.787%. Mühle et al. [30] did experimental investigation on a two bladed rotor with two interchangeable wing tips. The first wing tip was like a regular wind turbine with straight-cut wingtip while the second wing tip was a downstream-facing winglet. They reported that an optimized winglet design can improve the energy extraction as well as accelerate the recovery of turbulent kinetic energy in the wake by quicker tip vortex interaction. Mourad et al. [31] computationally explored the effects of winglet geometry on horizontal axis wind turbines. They found that downwind winglets with toe angles from 10° to 30° can reduce power outputs compared to rotors with no winglets.

Despite these progresses, the optimal control and designs of wind turbines to achieve the best performance under various incoming flow conditions remain a challenge. Specifically, there has been little investigations on the active/passive pitching of winglets, which may provide novel approaches for altering the aerodynamic characteristics of blades and protect turbines in extreme wind conditions. In this work, we explored the possibility of adjusting the performance of a wind turbine with winglets by changing its pitching angles. Wind tunnel experiments were designed to investigate how the variation of winglet pitching angles influences the aerodynamic loads, rotating speed, and wake characteristics of a modeled turbine. Results of this work will shed lights on reducing the thrust force and turbine rotating speed under strong wind, and estimating its influence on the performance of downstream turbines. The paper is organized as follows. The experimental setup is illustrated in Section 2; main results and analysis are detailed in Section 3, and final conclusions are summarized in Section 4.

## 2. Experimental Setup

Model wind turbines with winglets under various pitching angles were placed on the bottom wall of the Boundary Layer and Subsonic Tunnel (BLAST) in the University of Texas at Dallas. The test section of BLAST is 30 m long, 2.1 m high, and 2.8 m wide; during the experiment, incoming air flow temperature was controlled by a cooling system and maintained within 22.5 ± 0.3 °C to ensure constant incoming air properties. In order to well develop the turbulent boundary layer (TBL) for turbines, cubic blocks with 2.5 cm height located 0.2 m between each other were placed on the bottom surface of the test section (Figure 1a). The rotation frequency of the fan of BLAST was fixed at 120 Hz; this leads to the mean velocity of incoming flow at hub height of the turbine as $U_{hub}$ = 6.43 m s$^{-1}$ where the turbulence intensity is $I_u = \sigma_u/U_{hub}$ = 12%, which is similar to those observed with full-scale turbines [32]. Here, $\sigma_u$ denotes the standard deviation of the streamwise velocity. The TBL reaches the freestream velocity at $z \approx$ 55 cm and therefore boundary layer thickness of $\delta/z_{hub} \approx 2.75$. Details for the non-dimensional profiles of the incoming velocity $U/U_{hub}$, streamwise turbulence intensity $\sigma_u/U_{hub}$ and kinematic shear stress $-\overline{u'v'}/U_{hub}^2$ within the TBL are presented in Figure 2.

The horizontal-axis wind turbines were designed on a base model from Sandia National Labs [33,34] and manufactured from the Stratasys F370 3D printer in University of Texas at Dallas. All modeled turbines share the same rotor diameter of $d_T$ = 200 mm and the hub height $z_{hub}$ = 200 mm, leading to a Reynolds number of $Re = U_{hub}d_T/\nu = 1.3 \times 10^5$; here, $\nu$ is the kinematic viscosity of air. The turbine tower was made from the M5 threaded rod. Details of the turbine blade geometry across various sections are provided in Tobin et al. [9,27] and not duplicated here briefly. The blockage ratio of the turbine was 0.53% based on the rotor sweeping area and wind tunnel cross section, which led to neglectable blockage effects. In this work, special attention is focused on the influence of winglet pitching on the wake and turbine performance. The winglets were designed by extending the blade's tip with $l_w$ = 8 mm (4% of rotor diameter) in a plane perpendicular to that of the rotor. Here, the geometry of the winglet is a rectangular plate with its width $b_w$ the same as the blade tip (Figure 1c,d) and resembles a wing-tip flap. It is worth pointing out that the winglet length tested here is slightly longer than those applied in other works [27,29]; this is limited by the resolution of force/flow measurements where longer winglet facilitates to highlight the influence of its pitching in altering the turbine performance and wakes. The pitching angle of the winglets $\alpha$ is defined by the angle between blade tip edge and the surface of winglets (Figure 1b). In this work, four winglet pitching angles with $\alpha$ = 0°, 30°, 60° and 90° were investigated. A 24 mm-diameter DC motor from RS PRO with a constant resistance through the experiments was used as the loading to control the rotating speed [11,27,35]. This led to the tip-speed-ratio (TSR) of $\lambda = 2\pi\omega R/U_{hub} \approx 4.2$ for the base case ($\alpha$ = 0°), where $R$ is the turbine radius. The measured power coefficient for the base case is $C_p \approx 0.127$. Both TSR and $C_p$ from current work are close to previous studies with similar rotor design [9,11,27]. The instantaneous turbine rotating speed was inferred from the output voltage of the DC motor measured directly via a USB-6210 datalogger from National Instruments (Austin, TX, USA). For each experiment, the voltage was sampled at a frequency of 10 kHz for a period of 100 s. Complementary measurements of time-averaged aerodynamic loads were performed with an ATI high-resolution force sensor connected to the turbine tower. The sensor was embedded within the bottom roughness to avoid any disturbs on the wake development. During each experiment, the instantaneous thrust forces were captured at a frequency of 1 kHz for periods of 60 s. The uncertainty of the sensor was less than 1.2% according to the minimum measured thrust.

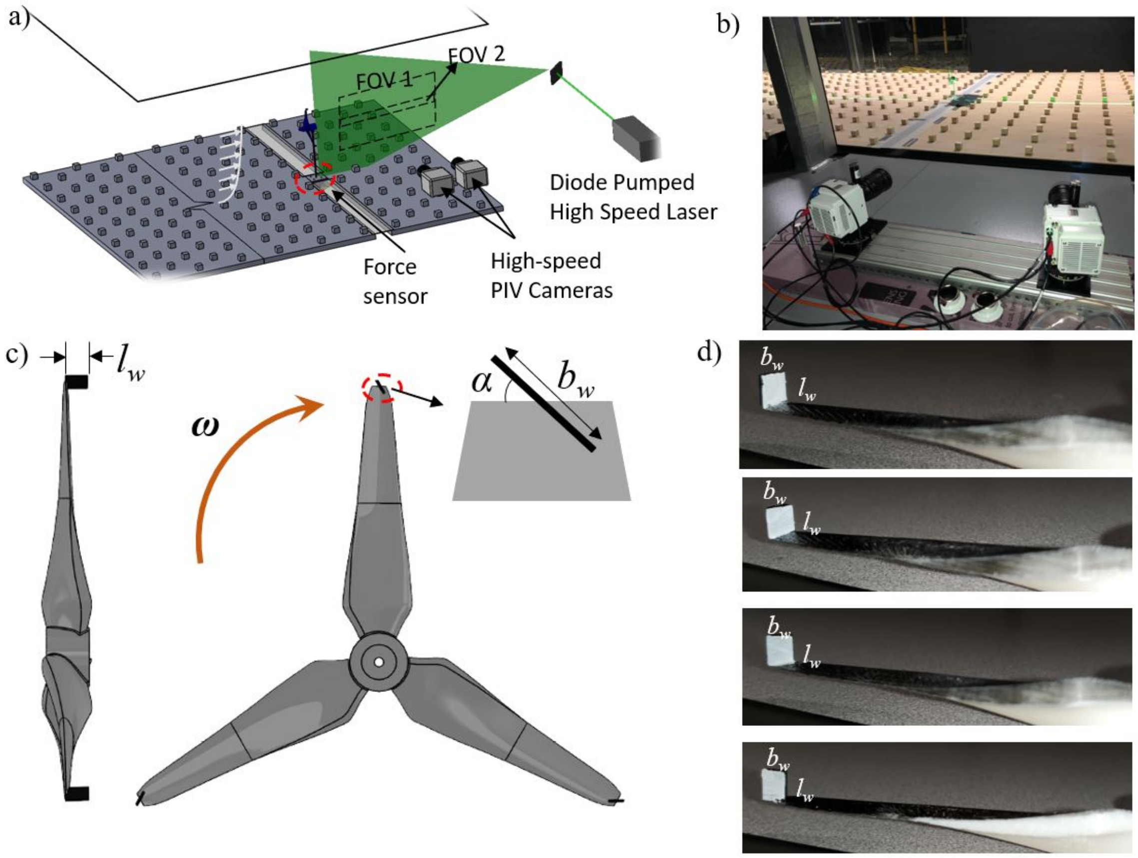


**Figure 1.** (**a**) schematic of the experimental setup illustrating the PIV system, force sensor, and bottom wall roughness; (**b**) photograph of the experimental setup in BLAST; (**c**) details of the turbine rotors highlighting the definition of winglet pitching angle from lateral (left) and leeward (right) side views. The orange arrow indicates the clockwise direction of turbine rotation from the leeward sight; (**d**) photographs of blade tips with winglet with pitching angles at $\alpha = 0°, 30°, 60°$ and $90°$ (from top to bottom). The leeward surface of the turbine was painted black and the winglet was paint white.

The incoming TBL and wake statistics along central axis of each turbine were characterized by a time-resolved particle image velocimetry (PIV) system from TSI. Two high-speed Phantom VEO440 cameras with 4 MP (2560 × 1600 pixels) resolutions were horizontally aligned to create a combined field of view (FOV 1) of 500 mm × 340 mm which includes ~20 mm gap to investigate the mean wake flows. The FOV was located at the turbine wake region within streamwise distances $x/d_T \in [1.85, 3.05]$, $[3.15, 4.35]$ and heights $z/z_{hub} \in [0.3, 2]$, where the coordinate system was defined with the origin coincident with the rotor plane at the bottom wall. For each experiment, 2500 image pairs were collected at a frequency of 30 Hz. The characterization of unsteady flow dynamics focuses on the wake region near the turbine hub height. Here, FOV 2 with the same streamwise regions but heights of $z/z_{hub} \in [0.8, 1.2]$ were explored, where the sampling frequency was set at 500 Hz with a period of 50 s (i.e., 25,000 image pairs) to capture the instantaneous wake fluctuations. This sampling frequency is constrained by the storage of the PIV camera; as will be shown in the following analysis, this frequency allows for well characterizing both energy containing and inertial sub-range of turbulent flows. For both mean and unsteady wake measurements, the FOVs were illuminated by a 1 mm thick laser sheet generated from a 30 mJ/pulse laser, where air flow was seeded by 15 µm-diameter soap bubbles from the TSI bubble generator. The soap bubbles were well mixed by the recirculating wind tunnel before each experiment. The image pairs were processed using an Insight4G software package (Version: 11.1.1.0 TSI, Shoreview, MN, USA) from TSI with a multipass scheme. The final interrogation window size was 32 × 32 pixels with 50% overlap, resulting in a final vector grid spacing $\Delta x = \Delta y = 2.4$ mm. The overall uncertainty of the identified seeding particle locations was ~0.1 pixel [36]; this led to the uncertainty of flow velocity measurement of ~1.4% given the bulk particle displacement of 7 pixels between two successive images.

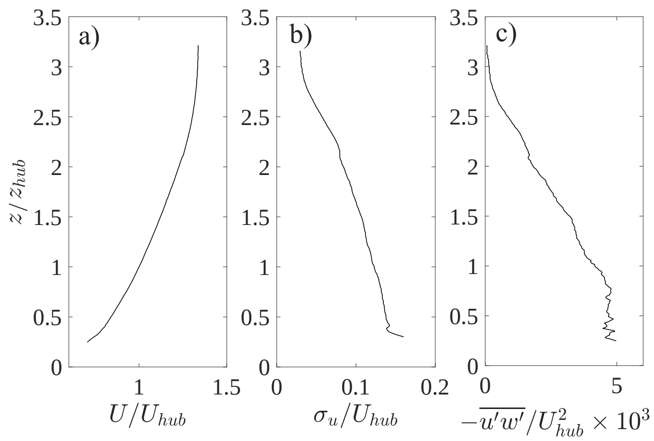


**Figure 2.** Main characteristics of the incoming turbulent boundary layer flow. (**a**) time-averaged velocity $U/U_{hub}$; (**b**) streamwise turbulence intensity $\sigma_u/U_{hub}$; (**c**) kinematic shear stress $-\overline{u'v'}/U_{hub}^2$. The vertical distances are normalized by the turbine hub height $z_{hub}$.

## 3. Results and Discussion

In this section, we discuss in detail the distinctive influences of blade winglet pitch angles on the statistics of turbine rotation speed, thrust coefficients, and wake development of the model wind turbines.

### *3.1. Rotation Speed and Thrust Force*

Specific insight on the effect of winglet pitch angles on the turbine rotation speed can be obtained from the mean and associated fluctuation statistics in each case.

Figure 3 shows a comparison between time-averaged tip-speed-ratio $\lambda$ and thrust coefficient $C_T$ under all different $\alpha$ normalized by that of the base case ($\alpha = 0°$), $\lambda_o = 4.2$, and $C_{T_o} = 0.585$. Here, the thrust coefficient is defined as

$$C_T = \frac{2T}{\rho_a \pi R^2 U_{hub}^2} \tag{1}$$

where $T$ is the mean thrust force and $\rho_a$ is the air density. Generally, with the growth of winglet pitching angle, $\lambda$ presented distinctive decrease up to ~28% under $\alpha = 60°$ and $90°$. The evolution of $C_T$ shows a similar trend where the maximum decrease reached ~20%. The power coefficients of turbines with $\alpha = 30°, 60°$ and $90°$ reduced to 0.088, 0.067, and 0.066, respectively.

As a dominant impact, with the growth of winglet pitching, its projected area impinged by the induced velocity due to turbine rotation increased monotonously; this led to higher local drag on the blade tip region and slowed down the turbine rotations. Interestingly, continuous growth of $\alpha$ from $60°$ to $90°$ induced a minor influence on both $\lambda$ and $C_T$. This can be explained from two aspects. First, as pointed out in Modi et al. [37], the difference of drag coefficient for a flat plat inclined at $60°$ and $90°$ is small. In addition, the winglet pitching can alter the local flow characteristics with its schematics shown in Figure 3b. Here, with the growth of $\alpha$, the winglet can no longer block the tip vortices (red arrows) well, which reduces the blade efficiency. At the same time, due to turbine rotation, additional pressure difference is produced between the windward side (surface A) and leeward side (surface B) of the winglet; such pressure difference can trigger secondary flow motions (blue arrows) which enhances the tip vortices and further slows down the turbine rotation. Note that, with $\alpha \rightarrow 90°$, the secondary flow is nearly perpendicular to the blade edges and therefore no longer facilitates the tip vortices. It is worth pointing out that the mass of the winglet portion is only ~1.8% of the entire blade; therefore, compared to traditional pitching of the whole blade, the winglet pitching provides potential with a much faster response of turbines under instant variations of wind velocities. Specifically, with the same generator resistance load, our work demonstrated that the turbine rotation speed can remain constant under a ~40% increase of incoming wind velocity by adjusting the winglet pitching angle from 0° to 60°. This provides new approaches for efficiently protecting the turbines under extreme wind conditions.

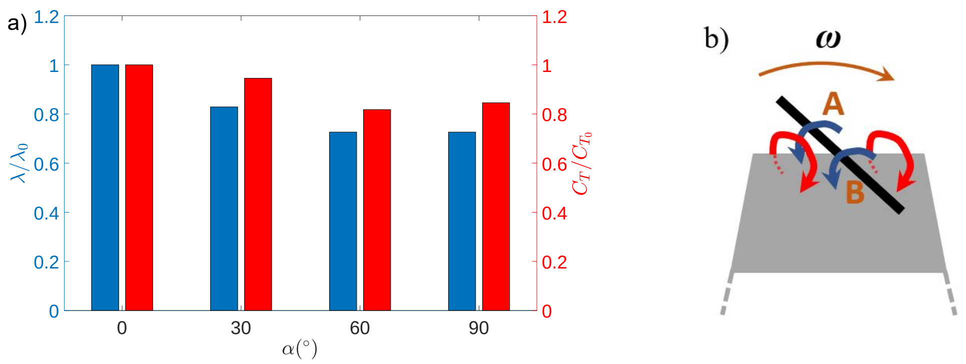


**Figure 3.** (**a**) comparison of the normalized mean tip speed ratio ($\lambda/\lambda_o$, blue bar) and thrust coefficient ($C_T/C_{T_o}$, red bar) of the turbine subjected to various winglet pitch angles; (**b**) schematic of the blade tip vortices with winglet pitching.

The influence of winglet pitching angles on turbine rotation speed fluctuations is illustrated in Figure 4; here, the power spectra ($\Phi_\omega$) of instantaneous rotation angular velocity $\omega$ are analyzed for selected cases, and the spectrum of incoming turbulence ($\Phi_u$) at turbine hub height is added in the subplot for discussion. In general, the spectra under 0° and 90° presented a similar trend including two distinctive regions. In the first region with $fd_T/U_{hub} < 0.06$ ($R_1$), the turbulence is within the range of energy containment, where the energy cascade decay of $\Phi_\omega$ is only related to the aerodynamic characteristics of the rotor [9,38]. Under higher frequency regions ($R_2$), the turbulence is within the inertial sub-range following $\Phi_u \propto f^{\frac{-5}{3}}$ which induced a faster decay rate of $\Phi_\omega$. For both winglet pitching angles, $\Phi_\omega$ plateaus at $fd_T/U_{hub} \sim 1$, indicating that the turbine rotation was no longer affected by the small scale turbulence. It is worth pointing out that both spectra presented minor differences in $R_2$, while, in general ,$\Phi_\omega$ of $\alpha$ = 90° showed lower energy under $R_1$. This reveals that the growth of winglet pitching angle reduces low-frequency turbine rotation speed fluctuations.

To further highlight the influence of winglet pitching angle on the rotation speed fluctuations in low-frequency regions, the integrated energy

$$\sigma_\omega^2(f) = \int_0^f \Phi_\omega(\epsilon)d\epsilon \quad (2)$$

was calculated as shown in Figure 5. Overall, small winglet pitching angles ($\alpha$ = 0° and 30°) led to larger $\sigma_\omega^2$ across all frequency ranges, corresponding to the higher $\Phi_\omega$ found in Figure 4. Note that, for all investigated $\alpha$, the curves of $\sigma_\omega^2$ plateaus at $fd_T/U_{hub} \approx 0.06$, i.e., the beginning of $R_2$, indicating that turbine rotation fluctuations are mostly modified by low-frequency components.

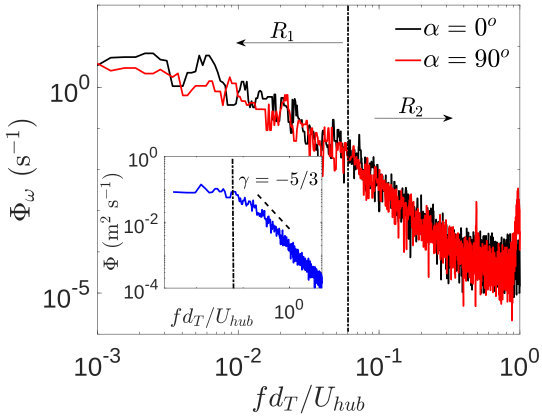


**Figure 4.** Spectra of instantaneous turbine rotation speed $\Phi_\omega$ under different $\alpha$. The subplot shows the spectra of incoming velocity at hub height. The vertical dashed line separates the turbulence from energy containing sub-range ($R_1$) to inertial sub-range ($R_2$).

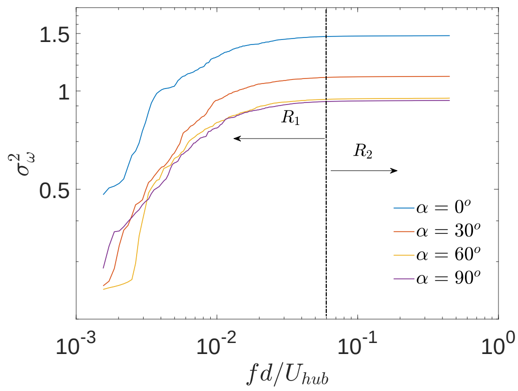


**Figure 5.** Integrated energy $\sigma^2_\omega$ of large-scale rotation speed fluctuations subjected to various $\alpha$.

## 3.2. Wake Characteristics

The influence of winglet pitching on the wake development is first assessed by comparing the normalized mean streamwise velocity distributions $U/U_{hub}$ shown in Figure 6. In general, under higher $\alpha$, the wake velocity deficit is reduced especially at the hub height region. Such phenomena are more clearly illustrated with the selected velocity deficit profiles $\Delta U = U_{inc}(z) - U(z)$ in Figure 7, where $U_{inc}$ is the time-averaged incoming flow speed. It proves that, in the very near wake $x/d_T \approx 2$, the wake recovering is not yet affected by the winglet pitching angles, while distinctive differences of wake velocities occur at $x/d_T \approx 3$ and gradually diminish in the far wake. It is worth pointing out that the induced velocity deficit is highly coupled with the thrust coefficient of the turbines; to better analyze the relation between aerodynamic loads and wake recovering, the Bastankhah and Porté-Agel's [39] analytical wake model is included to compare with our measurements. This model applied mass and momentum conservation to a control volume around a turbine with an assumption of self-similarity for the wake velocity profiles as:

$$\frac{\Delta U}{U_{hub}} = (1 - \sqrt{1 - \frac{C_T}{8A^2}})exp(-\frac{1}{2A^2}[(\frac{z - z_{hub}}{d_o})^2 + (\frac{y}{d_o})^2]) \quad (3)$$

where $y$ and $z$ are spanwise and vertical coordinates, and $A$ represents the wake development in streamwise direction as:

$$A = k^* x/d_T + 0.2\sqrt{\beta} \quad (4)$$

where $k^*$ is the wake growth rate, and $\beta$ is a function of $C_T$, given as:

$$\beta = \frac{1 + \sqrt{1 - C_T}}{2\sqrt{1 - C_T}} \tag{5}$$

In this work, specific attention is focused on the wake development in the turbine hub height where the influence of winglet pitching is most distinctive. Therefore, Equation (3) can be simplified with $z = z_{hub}$ and $y = 0$:

$$\frac{U}{U_{hub}} = \sqrt{1 - \frac{C_T}{8A^2}} \tag{6}$$

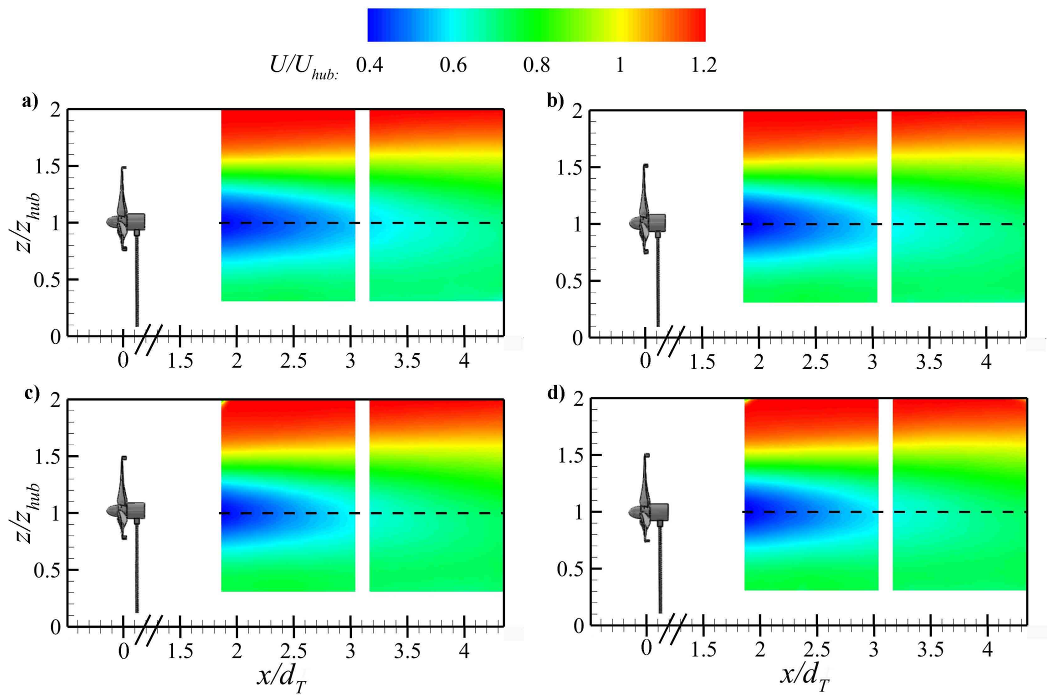


**Figure 6.** Normalized mean streamwise velocity distribution, $U/U_{hub}$, in the central plane for the turbines with winglet pitch angle under $\alpha$ = (**a**) 0°, (**b**) 30°, (**c**) 60°, and (**d**) 90°.

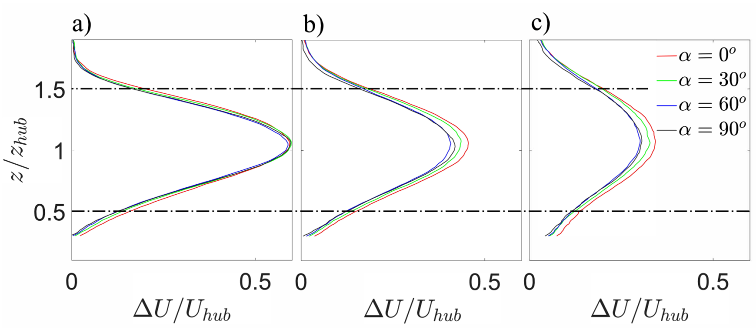


**Figure 7.** Profiles of normalized mean streamwise velocity deficit, $(U_{inc} - U)/U_{hub}$, for the wake flow at $x/d_T$ = (**a**) 2, (**b**) 3, and (**c**) 4 . The dash-dotted lines refer to positions of the upper and lower blade tips.

The comparison between measured (solid line) and modeled (dashed line) hub-height wake velocities are summarized in Figure 8. Key to determine the wake recovery rate is estimating the value of $k^*$. Previous works have shown that $k^*$ is a complex function of incoming turbulence and turbine designs [40,41]. In this work, $k^*$ is determined via complementary experiments of a turbine without winglet, where the wake flows and thrust forces were measured; this information is presented in

Figure 8b, which shows that $k^*$ = 0.0324 is the best fit for the wake development. Note that $C_T$ = 0.5744 for the turbine without winglet and is slightly lower than the base case, which follows the same trend as reported in Tobin et al. [27]. In addition, Bastankhah and Porté-Agel [39] pointed out that the velocity deficit profiles present a self-similar shape after a certain downstream distance ($x/d_T \gtrsim 3$); therefore, the model is compared with experimental results only at the second FOV ($x/d_T \geq 3.15$). In general, the model well presented the wake recovery trend under the influence of winglet pitching. Based on the model prediction, the winglet pitching from $\alpha$ = 0° to 60° produces ~6% higher hub-height wake velocity at $x/d_T$ = 5 and ~3.5% at $x/d_T$ = 7; with a first order approximation of $P \sim U^3$, this benefits the power production of downstream turbines with 19% and 11% located at $x/d_T$ = 5 and 7, respectively. It is worth pointing out that, for all investigated configurations, especially under high $\alpha$, this model led to a somewhat slower wake recovery rate $dU/dx$ prediction compared to the experimental results (Table 1). This indicates that, compared to traditional turbines sharing the same thrust coefficient, the pitching of winglet brings additional influence on wake recovery and induced stronger wake mixing to accelerate flow recovery [42,43].

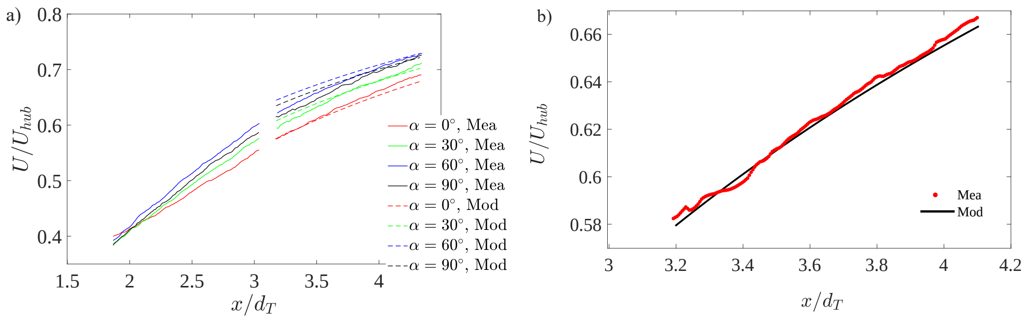


**Figure 8.** (**a**) normalized stream-wise mean velocity profile, $U/U_{hub}$ along the hub height for various $\alpha$. The solid lines represent those measured from experiment and the dashed lines are velocities predicted by model from Bastankhah and Porté-Agel [39]; (**b**) determination of $k^*$ by fitting the measured and modeled velocities of a traditional turbine without winglet.

**Table 1.** Comparison of measured and modeled $\frac{d(U/U_{hub})}{d(x/d_T)}$ across various pitching angles.

| | $\alpha$ = 0° | $\alpha$ = 30° | $\alpha$ = 60° | $\alpha$ = 90° |
|---|---|---|---|---|
| $\frac{d(U/U_{hub})}{d(x/d_T)}$ (Mea) | 0.100 | 0.097 | 0.091 | 0.097 |
| $\frac{d(U/U_{hub})}{d(x/d_T)}$ (Mod) | 0.0893 | 0.0812 | 0.0724 | 0.0747 |

The quantification of wake fluctuations provides insights for estimating the unsteadiness of power outputs of downstream turbines; this information is characterized by the turbulence kinetic energy $TKE = \langle u'^2 + w'^2 \rangle / 2U_{hub}^2$ shown in Figure 9; here, $u'^2$ and $w'^2$ are the velocity fluctuations in streamwise and spanwise directions and $\langle . \rangle$ denotes the time-average. Due to the limitation of two-dimensional PIV measurement, the velocity fluctuations in the $y$-axis component is not included [35,44]. This quantity illustrates the strong fluctuations of wake velocity due to the influence of $\alpha$. Overall, distinctive wake fluctuations occur near the top-tip regions of the turbine where the mean velocity shear is significant; such phenomenon is similar to those observed in traditional turbine wakes from both numerical simulations and experiments [45,46]. It is worth pointing out that high $\alpha$ induces a distinctive increase of $TKE$ in the hub-height region, especially within the near wake; this is more clearly shown by the $TKE$ distribution profiles in Figure 10, where the difference of $TKE$ across various $\alpha$ reaches the maximum at $x/d_T = 2, z/z_{hub} \approx 1.2$ and gradually diminishes along the streamwise direction. To further investigate the production of strong $TKE$ under high $\alpha$, wake fluctuations normalized by hub-height incoming velocity at streamwise ($I_u$) and vertical ($I_v$) directions are analyzed as shown in Figures 11 and 12 for selected cases. While the variation of $\alpha$ induced little influence on the distribution of $I_u$ (Figure 11), higher $\alpha$ produced significantly stronger vertical flow fluctuations especially near the hub-height region within $x/d_T \lesssim 3$ (Figure 12); this contributed to the overall stronger $TKE$ shown in Figure 9.

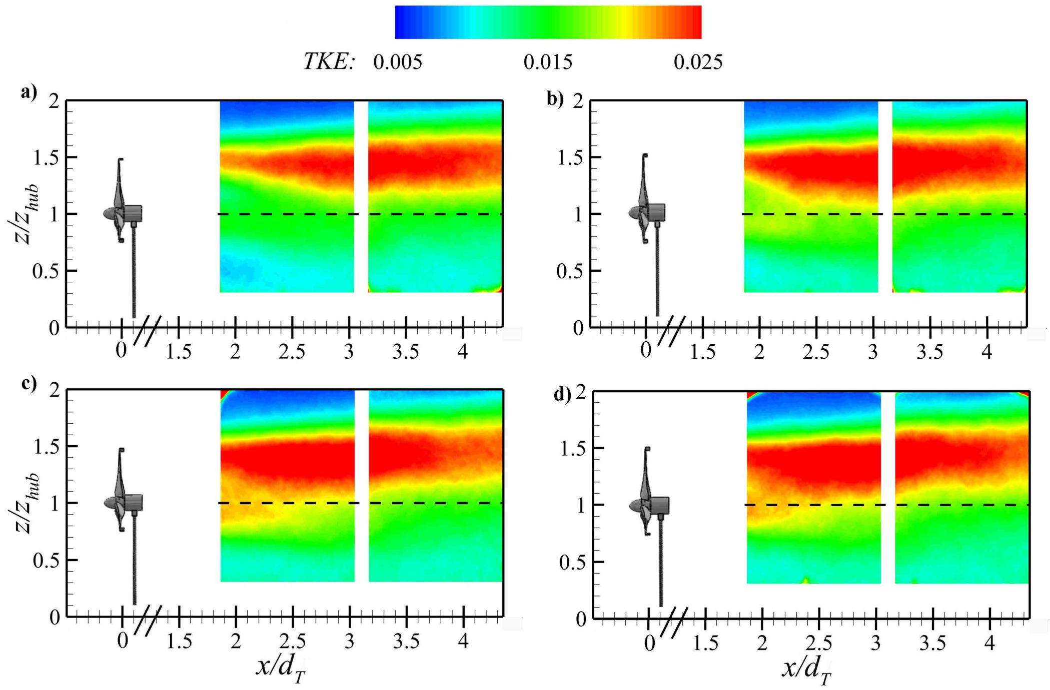


**Figure 9.** Distribution of turbulence kinetic energy, $TKE = < u'^2 + w'^2 > /2U_{hub}^2$, in the central plane for the turbines under $\alpha$ = (**a**) 0°, (**b**) 30°, (**c**) 60° and (**d**) 90°.

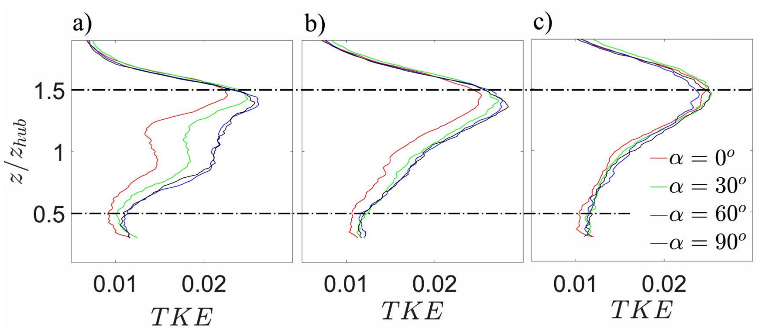


**Figure 10.** Profiles of turbulence kinetic energy, for the wake flow at $x/d_T$ = (**a**) 2, (**b**) 3, and (**c**) 4.

Insights on the influence of $\alpha$ for the structure of turbulence may be characterized by the difference between pre-multiplied streamwise velocity spectra in the wake and incoming flow at hub height along the stream-wise direction shown in Figure 13, which is given as

$$\Delta(f\phi) = f\phi|_{wake} - f\phi|_{inc} \tag{7}$$

where $f$ is the frequency and $\Phi$ is the corresponding energy spectra of flow velocity. Overall, across all $\alpha$, the turbines increased turbulent motions within $fd_T/U \gtrsim 10^{-1}$ and suppressed wake fluctuations with larger scales; similar 'high-pass filtering' effects of turbines on the wake flows were observed in previous experimental work [47]. Interestingly, for the very near wake flow ($x/d_T \lesssim 3$), such suppression is most distinctive under $\alpha = 0°$ but gradually diminishes with the growth of $\alpha$. As discussed in Figure 3, the winglet pitching significantly reduces the tip-speed-ratio and therefore the blades became less 'efficient' in 'high-pass filtering' the wake flows, especially in the very near wake regions.

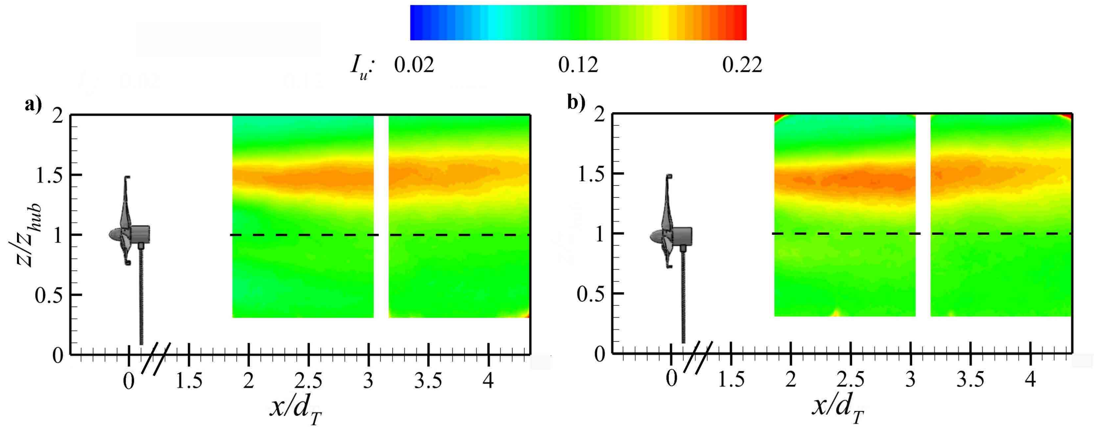


**Figure 11.** Normalized streamwise wake velocity fluctuation $I_u$ under $\alpha$ = (**a**) 0° and (**b**) 90°. The dash-dotted lines refer to positions of the upper and lower blade tips.

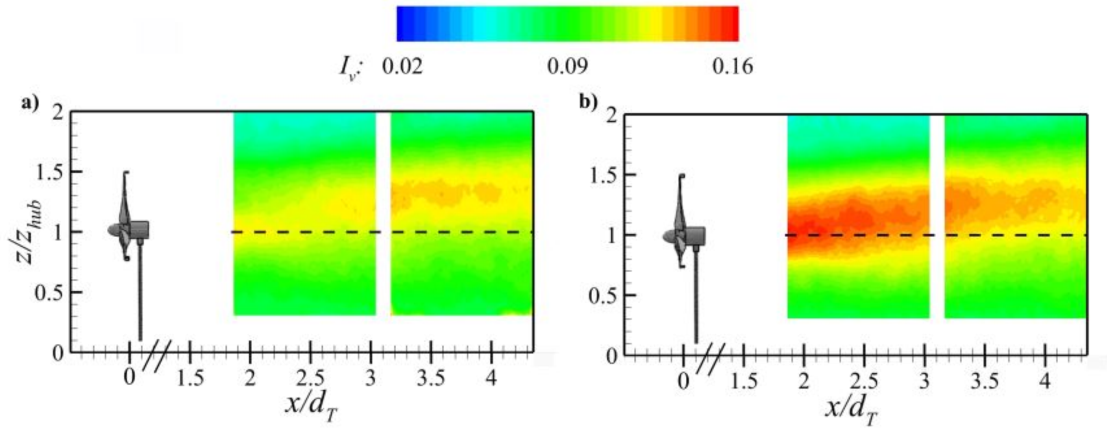


**Figure 12.** Normalized streamwise wake velocity fluctuation $I_v$ under $\alpha$ = (**a**) 0° and (**b**) 90°.

Finally, we discuss the wake turbulence transport under different winglet pitching; this helps to analyze the correlation of power output fluctuations between upstream and downstream turbines [11]. This quantity is analyzed by the cross-correlations on the time-series of streamwise velocities at two locations:

$$\eta(\tau)|_{2d_T,2d_T+\delta x} = \langle u_{2d_T}(t) u_{2d_T+\delta x}(t+\tau) \rangle \tag{8}$$

Equation (8) describes the coherent motions between flow velocities at $x = 2d_T$ and downstream locations $x = 2d_T + \delta x$ along the hub-height. Selected cases for the evolution of $\eta$ are shown in Figure 14a. It is clear that, with a specific time delay ($\Delta t$), the value of $\eta$ reaches the local maximum as highlighted by the red dashed lines, where the footprint of upwind flow fluctuations is transported to the downstream locations. As expected, with longer distance (i.e., higher $\delta x$), the corresponding transportation time increased where the strength of correlation (i.e., maximum value of $\eta$) decreased. To further investigate the influence of $\alpha$ on the wake transport speed, the distribution of $\Delta t$ normalized by $\delta x$ and $U_{hub}$ (i.e., the ratio between averaged wake transport speed within the distance $\delta x$ and the incoming velocity) across various $\alpha$ and $\delta x$ is summarized in Figure 14b. Interestingly, the wake transport speed is in general higher than the time-averaged wake velocity at the turbine hub height ($U/U_{hub}$) from Figure 8), especially under high $\alpha$ cases. This further highlighted that the pitching of winglet facilitates the wake mixing, where the wake transport is not barely determined by the local wind velocity but also influenced by the mixing with the surrounding background TBL, which is always higher than the local wake flow velocities [48].

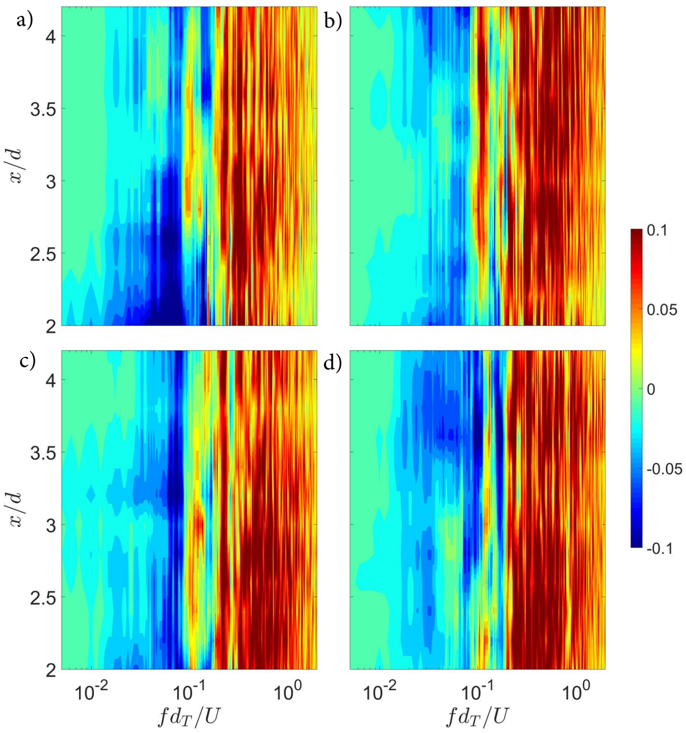


**Figure 13.** Compensated velocity spectra difference $\Delta(f\phi)$ normalized by its local maximum between the wake and incoming flow for $\alpha$ = (**a**) 0°, (**b**) 30°, (**c**) 60°, and (**d**) 90° .

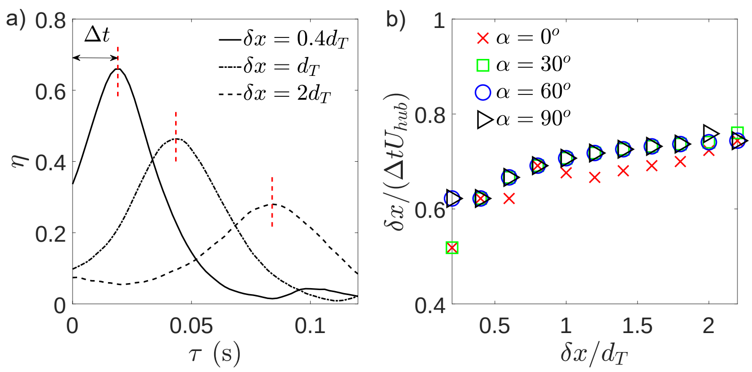


**Figure 14.** (**a**) cross-correlation function $\eta(\tau)$ for selected case under $\alpha$ = 0°; (**b**) normalized time-delay of wake transport across various downstream distances and $\alpha$.

## 4. Conclusions

In this study, the influence of winglet pitching as an aero-brake on the performance and wake characteristics of a modeled turbine was investigated with wind tunnel experiments. Despite a small part of the entire blade (4% of turbine diameter length), the pitching of winglet can significantly alter the turbine rotation speed, thrust coefficients, wake recovery rate, and turbulence transport. Key concluding points in this work are summarized as follows:

(i) The pitching of winglets can effectively decrease the turbine rotation speed and thrust coefficient up to ~28% and ~20% as the pitching angle is increased to 60°. The unsteady turbine rotations are dominated by the low-frequency fluctuations, which can be suppressed under large winglet pitching angles.

(ii) The pitching of winglet leads to smaller velocity deficit which is induced by both the variation of thrust coefficient and blade aerodynamic features. The growth of winglet pitching angle significantly increases the vertical velocity fluctuations; this is clearly reflected by the distinctively higher turbulence kinetic energy at hub height of the near wake regions.

(iii) Large winglet pitching angles reduce the high-pass filtering effects of wake fluctuations in the near wake. While the mean wake velocity presents distinctive variation at the hub-height along the streamwise direction, the speed of wake fluctuation transport under large winglet pitching angles demonstrates much smaller changes.

To sum up, this work provided evidence that, for turbines with winglets, altering their pitching angles can effectively adjust the turbine performance, influencing the wake flows and therefore downstream turbine operations. This concept is similar to the control of flaps which changes the local aerodynamic characteristics of the blades. Future work will explore in detail the influence of winglet lengths and shapes, as well as the possibility of applying different winglet pitching angles on each blade to balance the induced torque acting on the hub due to nonuniform incoming flows.

**Author Contributions:** E.J.A. and D.B.S. conducted the experiments, E.J.A. prepared the manuscript and Y.J. guided the work and revised the manuscript. All authors contributed to the data analysis. All authors have read and agreed to the published version of the manuscript.

**Funding:** This research received no external funding.

**Acknowledgments:** This work was supported by the Department of Mechanical Engineering, the University of Texas at Dallas, as part of the start-up package of Yaqing Jin.

**Conflicts of Interest:** The authors declare no conflict of interest.

## References

1. Electricity in the United States-Energy Explained, Your Guide To Understanding Energy (EIA, 2019). Available online: https://www.eia.gov/energyexplained/index.cfm?page=electricity_in_the_united_states (accessed on 3 January 2020 ).
2. Cost and Performance Characteristics of New Generating Technologies, Annual Energy Outlook 2019. U.S. Energy Information Administration. Available online: https://www.eia.gov/outlooks/aeo/assumptions/pdf/table_8.2.pdf (accessed on 3 January 2020 ).
3. Barthelmie, R.; Hansen, O.F.; Enevoldsen, K.; Højstrup, J.; Frandsen, S.; Pryor, S.; Larsen, S.; Motta, M.; Sanderhoff, P. Ten years of meteorological measurements for offshore wind farms. *J. Sol. Energy Eng.* **2005**, *127*, 170–176. [CrossRef]
4. Pryor, S.C.; Barthelmie, R.J. Flow characteristics in the coastal zone. In *European Seminar Offshore Wind Energy in Mediterranean and Other European Seas*; ENEA: Paris, France, 2000; pp. 29–43.
5. Akpinar, E.K.; Akpinar, S. An assessment on seasonal analysis of wind energy characteristics and wind turbine characteristics. *Energy Convers. Manag.* **2005**, *46*, 1848–1867. [CrossRef]
6. Gökçek, M.; Bayülken, A.; Bekdemir, S. Investigation of wind characteristics and wind energy potential in Kirklareli, Turkey. *Renew. Energy* **2007**, *32*, 1739–1752. [CrossRef]
7. Guo, H.; Xu, M.; Hu, Q. Changes in near-surface wind speed in China: 1969–2005. *Int. J. Climatol.* **2011**, *31*, 349–358. [CrossRef]
8. Ouammi, A.; Dagdougui, H.; Sacile, R.; Mimet, A. Monthly and seasonal assessment of wind energy characteristics at four monitored locations in Liguria region (Italy). *Renew. Sustain. Energy Rev.* **2010**, *14*, 1959–1968. [CrossRef]
9. Tobin, N.; Zhu, H.; Chamorro, L.P. Spectral behaviour of the turbulence-driven power fluctuations of wind turbines. *J. Turbul.* **2015**, *16*, 832–846. [CrossRef]
10. Jin, Y.; Liu, H.; Aggarwal, R.; Singh, A.; Chamorro, L.P. Effects of freestream turbulence in a model wind turbine wake. *Energies* **2016**, *9*, 830. [CrossRef]
11. Liu, H.; Jin, Y.; Tobin, N.; Chamorro, L.P. Towards uncovering the structure of power fluctuations of wind farms. *Phys. Rev. E* **2017**, *96*, 063117. [CrossRef]
12. Liu, H.; Hayat, I.; Jin, Y.; Chamorro, L. On the evolution of the integral time scale within wind farms. *Energies* **2018**, *11*, 93. [CrossRef]
13. Hau, E. Commercial Applications of Wind Turbines. In *Wind Turbines: Fundamentals, Technologies, Application, Economics*; Springer Science & Business Media: Munich, Germany, 2006; pp. 563–614.

14. Nagai, B.M.; Ameku, K.; Roy, J.N. Performance of a 3 kW wind turbine generator with variable pitch control system. *Appl. Energy* **2009**, *86*, 1774–1782. [CrossRef]
15. Muljadi, E.; Butterfield, C.P. Pitch-controlled variable-speed wind turbine generation. *IEEE Trans. Ind.* **2001**, *37*, 240–246. [CrossRef]
16. Gao, R.; Gao, Z. Pitch control for wind turbine systems using optimization, estimation and compensation. *Renew. Energy* **2016**, *91*, 501–515. [CrossRef]
17. Van Wingerden, J.W.; Hulskamp, A.W.; Barlas, T.; Marrant, B.; Van Kuik, G.A.M.; Molenaar, D.P.; Verhaegen, M. On the proof of concept of a 'smart' wind turbine rotor blade for load alleviation. *Wind Energy* **2008**, *11*, 265–280. [CrossRef]
18. Barlas, T.K.; van Kuik, G.A.M. Review of state of the art in smart rotor control research for wind turbines. *Prog. Aerosp. Sci.* **2010**, *46*, 1–27. [CrossRef]
19. Barlas, T.K.; Van der Veen, G.J.; Van Kuik, G.A.M. Model predictive control for wind turbines with distributed active flaps: Incorporating inflow signals and actuator constraints. *Wind Energy* **2012**, *15*, 757–771. [CrossRef]
20. Whitcomb, R.T. *A Design Approach and Selected Wind Tunnel Results at High Subsonic Speeds for Wing-Tip Mounted Winglets*; NASA TN D-8260; Natl. Aeronaut. Space Admin: Washington, DC, USA, 1976.
21. Johansen, J.; Sørensen, N.N. *Aerodynamic Investigation of Winglets on Wind Turbine Blades Using CFD Risø-R-1543(EN)*; Risø National Laboratory: Roskilde, Denmark, 2006.
22. Imamura, H.; Hasegawa, Y.; Kikuyama, K. Numerical analysis of the horizontal axis wind turbine with wihglets. *JSME Int. J. Ser. B Fluids Therm. Eng.* **1998**, *41*, 170–176. [CrossRef]
23. Gaunaa, M.; Johansen, J. Determination of the maximum aerodynamic efficiency of wind turbine rotors with winglets. *J. Phys. Conf. Ser.* **2007**, *75*, 012006. [CrossRef]
24. Saravanan, P.; Parammasivam, K.M.; Selvi Rajan, S. Pressure distribution of rotating small wind turbine blades with winglet using wind tunnel. *J. Sci. Ind. Res.* **2012**, *71*, 425–429.
25. Saravanan, P.; Parammasivam, K.M.; Selvi Rajan, S. Experimental investigation on small horizontal axis wind turbine rotor using winglets. *J. Eng. Appl.* **2013**, *16*, 159–164.
26. Belferhat, S.; Meftah, S.M.A.; Yahiaoui, T.; Imine, B. Aerodynamic Optimization of a Winglet Design. In *EPJ Web of Conferences*; EDP Sciences: Paris, France, 2013; Volume 45, p. 01010.
27. Tobin, N.; Hamed, A.M.; Chamorro, L.P. An Experimental Study on the Effects ofWinglets on the Wake and Performance of a ModelWind Turbine. *Energies* **2015**, *8*, 11955–11972. [CrossRef]
28. Zhu, B.; Sun, X.; Wang, Y.; Huang, D. Performance characteristics of a horizontal axis turbine with fusion winglet. *Energy* **2017**, *120*, 431–440. [CrossRef]
29. Khaled, M.; Ibrahim, M.M.; Hamed, H.E.A.; AbdelGwad, A.F. Investigation of a small Horizontal–Axis wind turbine performance with and without winglet. *Energy* **2019**, *187*, 115921. [CrossRef]
30. Mühle, F.; Bartl, J.; Hansen, T.; Adaramola, M.S.; Sætran, L. An experimental study on the effects of winglets on the tip vortex interaction in the near wake of a model wind turbine. *Wind Energy* **2020**, *23*, 1286–1300. [CrossRef]
31. Mourad, M.G.; Shahin, I.; Ayad, S.S.; Abdellatif, O.E.; Mekhail, T.A. Effect of winglet geometry on horizontal axis wind turbine performance. *Eng. Rep.* **2020**, *2*, e12101. [CrossRef]
32. Chamorro, L.P.; Lee, S.J.; Olsen, D.; Milliren, C.; Marr, J.; Arndt, R.; Sotiropoulos, F. Turbulence effects on a full-scale 2.5 MW horizontal-axis wind turbine under neutrally stratified conditions. *Wind Energy* **2015**, *18*, 339–349. [CrossRef]
33. Shiu, H.; Johnson, E.; Barone, M.; Phillips, R.; Straka, W.; Fontaine, A.; Jonson, M. A design of a hydrofoil family for current-driven marine-hydrokinetic turbines. In *International Conference on Nuclear Engineering*; American Society of Mechanical Engineers: New York, NY, USA, 2012; Volume 44984, pp. 839–847.
34. Johnson, E.; Fontaine, A.A.; Jonson, M.L.; Meyer, R.S.; Straka, W.A.; Young, S.; van Dam, C.P.; Shiu, H.; Barone, M. A1: 8.7 scale water tunnel test of an axial flow water turbine. In Proceedings of the 1st Marine Energy Technology Symposium, METS13, Washington, DC, USA, 10–11 April 2013; pp. 10–11.
35. Cheng, S.; Jin, Y.; Chamorro, L.P. Wind Turbines with Truncated Blades May Be a Possibility for Dense Wind Farms. *Energies* **2020**, *13*, 1810. [CrossRef]
36. Mao, Z.; Jin, Y.; Wang, Z.; Chamorro, L.P. On the Unsteady Wake of a Rigid Plate Under Constant Acceleration and Deceleration. *J. Fluids Eng.* **2020**, *142*, 051301 . [CrossRef]
37. Modi, V.J.; Wiland, E.; Dikshit, A.K.; Yokomizo, T. On the fluid dynamics of elliptic cylinders. *Int. J. Offshore Polar Eng.* **1992**, *2*, 267–280.

38. Jin, Y.; Ji, S.; Chamorro, L.P. Spectral Energy Cascade of Body Rotations and Oscillations under Turbulence. *Phys. Rev. E* **2016**, *94*, 063105. [CrossRef]
39. Bastankhah, M.; Porté-Agel, F. A new analytical model for wind-turbine wakes. *Renew. Energy* **2014**, *70*, 116–123. [CrossRef]
40. Abkar, M.; Sørensen, J.N.; Porté-Agel, F. An analytical model for the effect of vertical wind veer on wind turbine wakes. *Energies* **2018**, *11*, 1838. [CrossRef]
41. Archer, C.L.; Vasel-Be-Hagh, A.; Yan, C.; Wu, S.; Pan, Y.; Brodie, J.F.; Maguire, A.E. Review and evaluation of wake loss models for wind energy applications. *Appl. Energy* **2018**, *226*, 1187–1207. [CrossRef]
42. Campagnolo, F.; Petrović, V.; Bottasso, C.L.; Croce, A. Wind tunnel testing of wake control strategies. In Proceedings of the 2016 American Control Conference (ACC), Boston, MA, USA, 6–8 July 2016; IEEE: Piscataway, NJ, USA, 2016; pp. 513–518.
43. Annoni, J.; Gebraad, P.M.O.; Scholbrock, A.K.; Fleming, P.A.; van Wingerden, J.W. Analysis of axial-induction-based wind plant control using an engineering and a high-order wind plant model. *Wind Energy* **2016**, *19*, 1135–1150. [CrossRef]
44. Fu, S.; Jin, Y.; Zheng, Y.; Chamorro, L.P. Wake and power fluctuations of a model wind turbine subjected to pitch and roll oscillations. *Appl. Energ* **2019**, *253*, 113605. [CrossRef]
45. Wu, Y.T.; Porté-Agel, F. Atmospheric turbulence effects on wind-turbine wakes: An LES study. *Energies* **2012**, *5*, 5340–5362. [CrossRef]
46. Kang, S.; Yang, X.; Sotiropoulos, F. On the onset of wake meandering for an axial flow turbine in a turbulent open channel flow. *J. Fluid Mech.* **2014**, *744*, 376–403. [CrossRef]
47. Chamorro, L.P.; Guala, M.; Arndt, R.E.A.; Sotiropoulos, F. On the evolution of turbulent scales in the wake of a wind turbine model. *J. Turbul.* **2012**, *13*, 1–13.
48. Tobin, N.; Chamorro, L.P. Turbulence coherence and its impact on wind-farm power fluctuations. *J. Fluid Mech.* **2018**, *855*, 1116–1129. [CrossRef]